# Article

# Synthesis-on-substrate of quantum dot solids

Check for updates

Yuanzhi Jiang[1,2,10], Changjiu Sun[1,10], Jian Xu[3,10], Saisai Li[1,10], Minghuan Cui[4], Xinliang Fu[1], Yuan Liu[3], Yaqi Liu[5], Haoyue Wan[3], Keyu Wei[1], Tong Zhou[1], Wei Zhang[1,2], Yingguo Yang[6,7], Jien Yang[8], Chaochao Qin[4], Shuyan Gao[8], Jun Pan[9], Yufang Liu[4], Sjoerd Hoogland[3], Edward H. Sargent[3✉], Jun Chen[1,2✉] & Mingjian Yuan[1,2✉]

Perovskite light-emitting diodes (PeLEDs) with an external quantum efficiency exceeding 20% have been achieved in both green and red wavelengths[1–5]; however, the performance of blue-emitting PeLEDs lags behind[6,7]. Ultrasmall $CsPbBr_3$ quantum dots are promising candidates with which to realize efficient and stable blue PeLEDs, although it has proven challenging to synthesize a monodispersed population of ultrasmall $CsPbBr_3$ quantum dots, and difficult to retain their solution-phase properties when casting into solid films[8]. Here we report the direct synthesis-on-substrate of films of suitably coupled, monodispersed, ultrasmall perovskite QDs. We develop ligand structures that enable control over the quantum dots' size, monodispersity and coupling during film-based synthesis. A head group (the side with higher electrostatic potential) on the ligand provides steric hindrance that suppresses the formation of layered perovskites. The tail (the side with lower electrostatic potential) is modified using halide substitution to increase the surface binding affinity, constraining resulting grains to sizes within the quantum confinement regime. The approach achieves high monodispersity (full-width at half-maximum = 23 nm with emission centred at 478 nm) united with strong coupling. We report as a result blue PeLEDs with an external quantum efficiency of 18% at 480 nm and 10% at 465 nm, to our knowledge the highest reported among perovskite blue LEDs by a factor of 1.5 and 2, respectively[6,7].

Blue perovskite emitters are readily synthesized via halide substitution to produce Cl–Br mixed perovskites[9–13]; unfortunately, these are susceptible to halide segregation under electric field, resulting in spectral shifting[14]. Perovskite quantum dots (QDs) exhibit size-dependent optoelectronic properties, enabling tuning to blue emission: $CsPbBr_3$ QDs with size of 3–5 nm are required because the exciton Bohr diameter of $CsPbBr_3$ is 7 nm (refs. [15,16]). However, it has proven difficult to achieve monodispersed sub-5 nm-sized QDs via traditional colloidal synthesis[17]. During assembly into semiconducting solids, the surface ligands are readily lost upon ligand exchange, resulting in variable degrees of QD fusion and further increased polydispersity[8,18,19]. Consequently, ultrasmall $CsPbBr_3$ QDs have yet to produce efficient blue PeLEDs.

We reasoned that two key steps—ligand exchange and coupling during film formation—are particularly challenging when dealing with ultraconfined dots, leading as they do to redshift and increased emission linewidth. We therefore pursued a process that would avoid this approach to materials processing, seeking instead to unite synthesis and film fabrication into one step. However, to synthesize—in situ, on a range of substrates—perovskite QD solids that are monodispersed and suitably coupled, is notoriously challenging: the structure of the ligands influences the dimensionality of the assembled perovskites, producing variously three-dimensional networks, two-dimensional (2D) quantum wells and one-dimensional chains[20,21]. This motivated us to delve into how ligand structure can regulate synthesis-on-substrate (SoS) of perovskite QD films.

We began by noting that the ligand must be compact and conjugated to ensure inter-dot coupling. Layered perovskite precipitation must be prevented to provide pure cubic-lattice crystals. Further, strong ligand surface binding affinity is necessary to constrain cubic grain growth, a prerequisite to realizing a nanoparticle domain size that resides within the quantum confinement regime.

As a starting point, we began with conventional PEA⁺ (phenylethyl ammonium) ligands, a compact and conjugated ligand. We prepared precursor solution by mixing $PbBr_2$ and CsBr with PEA⁺ ligands in

[1]Key Laboratory of Advanced Energy Materials Chemistry (Ministry of Education), Renewable Energy Conversion and Storage Center (RECAST), College of Chemistry, Nankai University, Tianjin, P. R. China. [2]Haihe Laboratory of Sustainable Chemical Transformations, Tianjin, P. R. China. [3]Department of Electrical and Computer Engineering, University of Toronto, Toronto, Ontario, Canada. [4]Henan Key Laboratory of Infrared Materials and Spectrum Measures and Applications, College of Physics and Materials Science, Henan Normal University, Xinxiang, P. R. China. [5]College of Environmental Science and Engineering, Ministry of Education Key Laboratory of Pollution Processes and Environmental Criteria, Nankai University, Tianjin, P. R. China. [6]Shanghai Synchrotron Radiation Facility (SSRF), Zhangjiang Lab, Shanghai Advanced Research Institute, Chinese Academy of Sciences, Shanghai, P. R. China. [7]School of Microelectronics, Fudan University, Shanghai, P. R. China. [8]School of Materials Science and Engineering, Henan Normal University, Xinxiang, P. R. China. [9]College of Materials Science and Engineering, Zhejiang University of Technology, Hangzhou, P. R. China. [10]These authors contributed equally: Yuanzhi Jiang, Changjiu Sun, Jian Xu, Saisai Li. ✉e-mail: ted.sargent@utoronto.ca; chenabc@nankai.edu.cn; yuanmj@nankai.edu.cn
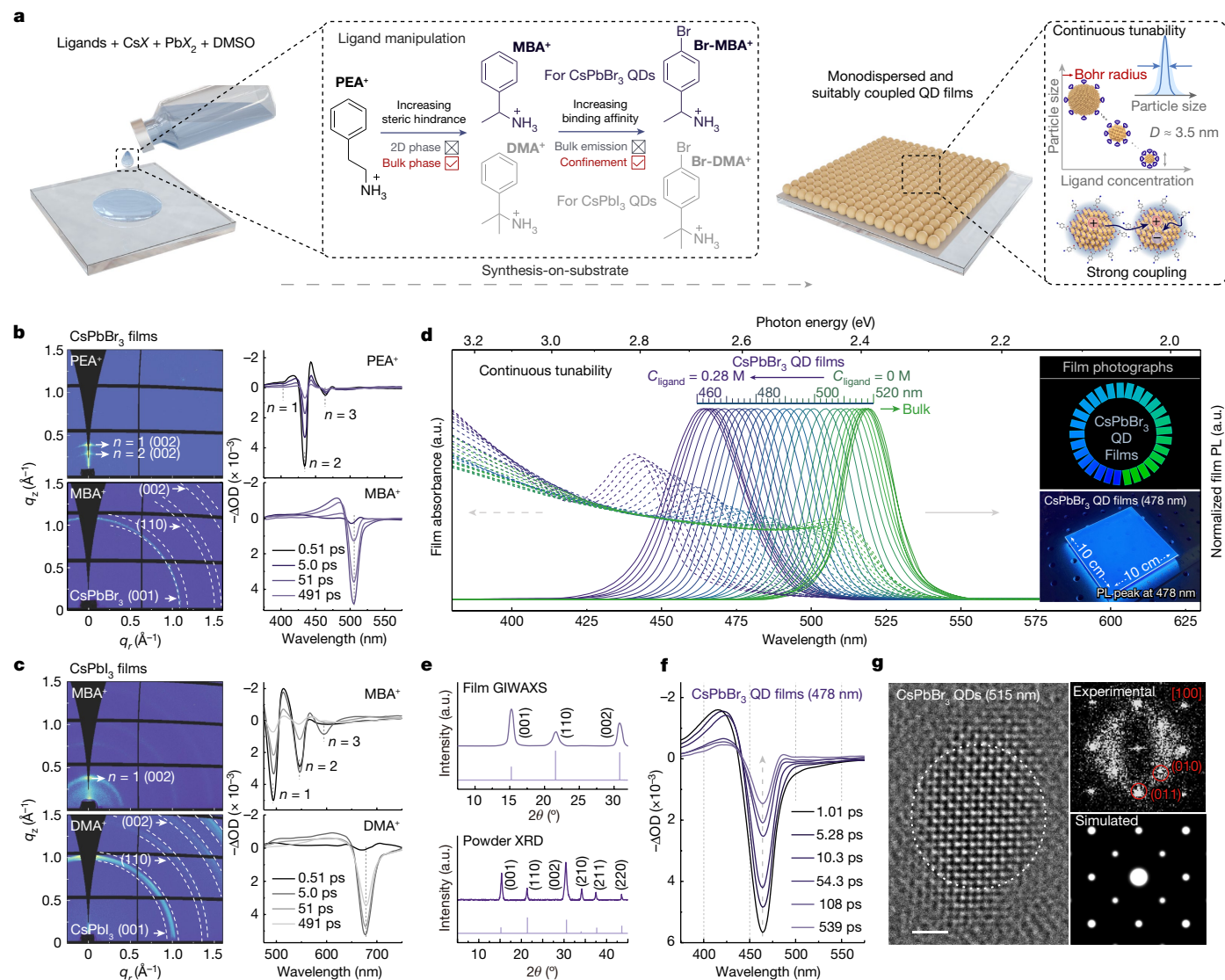
**Fig. 1 | Perovskite QD semiconducting solids. a**, Illustration of the approach. *D*, diameter. **b,c**, GIWAXS patterns and transient absorption spectra for CsPbBr₃ (**b**) and CsPbI₃ (**c**) films with different ligands. $q_z$, out-of-plane scattering vector; $q_r$, in-plane scattering vector; ΔOD, optical density variation. **d**, Photoluminescence (PL) and absorption spectra of CsPbBr₃ QD films with various ligands concentrations, $C_{ligand}$, from 0 to 0.28 M. Inset, photographs of QD films under excitation. **e**, GIWAXS pattern of CsPbBr₃ QD films (top) and XRD pattern of QD powders (bottom). In each, the pale purple line gives the simulated CsPbBr₃ results. **f**, Transient absorption spectra of QD films (478 nm). **g**, Low-dose HRTEM image and corresponding fast Fourier transform pattern of CsPbBr₃ projected along the [100] direction. The inset shows the simulated selected area electron diffraction (SAED) pattern. Scale bar, 2 nm.

dimethyl sulfoxide (DMSO). The resulting perovskite films are prepared via single-step spin-coating (Fig. 1a), followed by antisolvent dripping to initiate the crystallization. As expected, layered perovskites are observed in both grazing-incidence wide-angle X-ray scattering (GIWAXS) patterns and transient absorption spectra[22–24] (Fig. 1b).

To suppress layered perovskite formation, and noting that a high degree of octahedral distortion causes instability of the layered perovskite phase[25], we sought to instantiate severe octahedral distortion with the aid of sterically hindered ligands[26]. We would engineer the head group (for example, for PEA⁺, the alkyl-ammonium group in the phenyl ring is the head group) to this end. We developed in analogue of PEA⁺, α-methyl-benzyl-ammonium (MBA⁺), which contains an extra methyl substitution (–CH₃) in the methylene (–CH₂–) position of the head group (Fig. 1a). Only the three-dimensional cubic CsPbBr₃ phase is then observed in GIWAXS patterns and transient absorption spectra (Fig. 1b).

We examined the head-group effect in CsPbI₃ perovskite, a semiconductor that possesses enlarged [PbI₆]⁴⁻ octahedra compared to CsPbBr₃.

In this case, we observe layered perovskites when using MBA⁺ ligands (Fig. 1c): the octahedral distortion imposed by MBA⁺ is not enough (Supplementary Note 1). We added a further methyl substitution to the methine (=CH–) group, generating α,α-dimethyl-benzyl-ammonium (DMA⁺) ligands; the GIWAXS patterns and transient absorption spectra then showed only cubic CsPbI₃ (Fig. 1c).

Density functional theory (DFT) calculations (Extended Data Fig. 3) illustrate that sterically hindered ligands cause severe octahedral distortion, making layered perovskites unstable. The ligands do not penetrate into the lattice, but are instead prone to remain at the surface and function as capping ligands, enforcing the cubic phase CsPbBr₃/CsPbI₃.

The emission wavelength of the films that use the MBA⁺ ligands correspond to that of bulk CsPbBr₃ (Supplementary Note 1). We sought therefore to increase the surface binding affinity of the ligand using halide substitution to tune binding energy[27]. Pursuing halide substitution in the phenyl ring, we synthesized α-methyl-4-bromide-benzylammonium (Br-MBA⁺), with bromide substitution at the *para* position of the tail group compared to MBA⁺ (Fig. 1a).
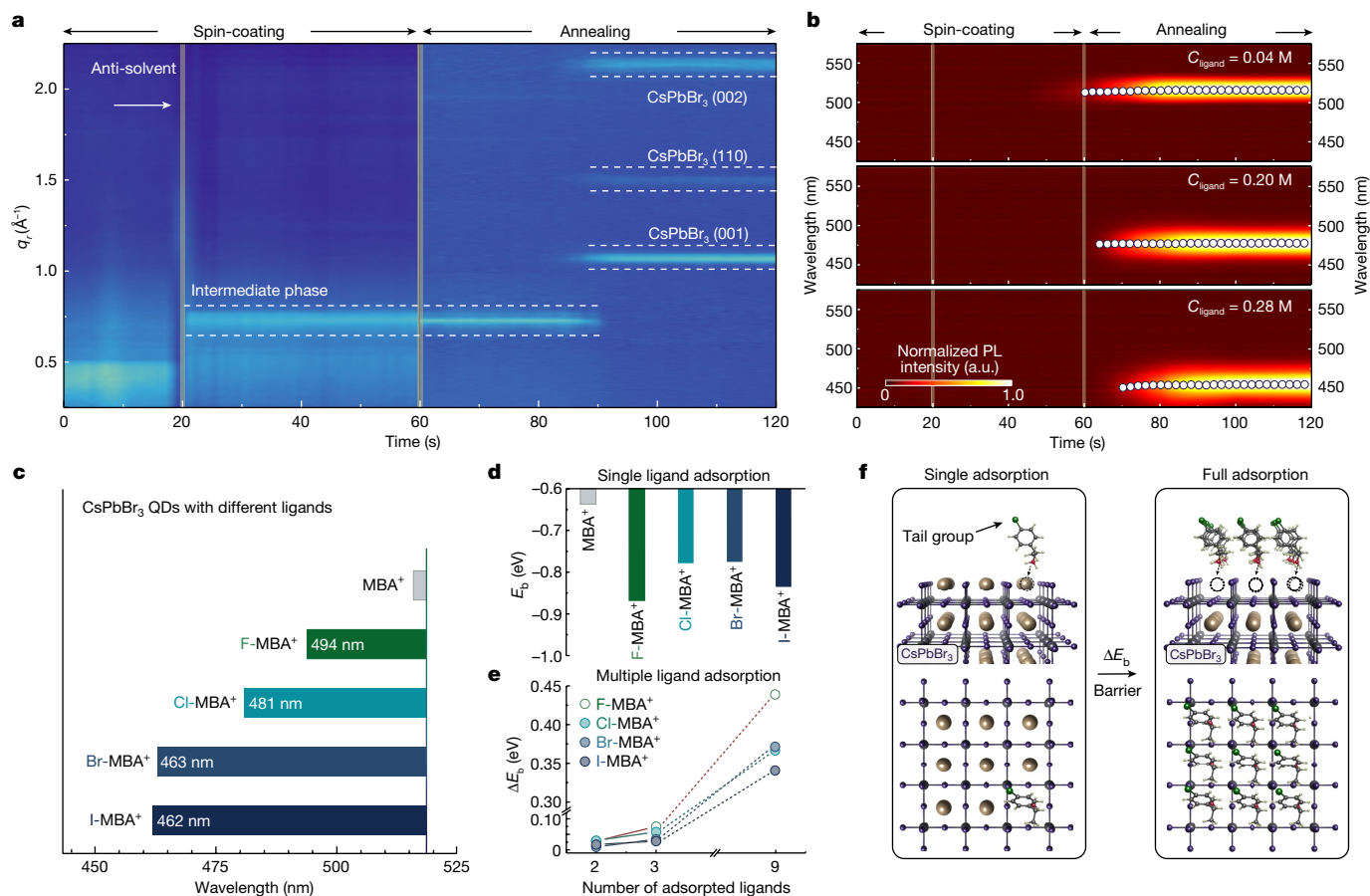
**Fig. 2 | Formation of SoS of QD films. a,b** In situ GIWAXS (**a**) and photoluminescence spectra (**b**) of the QD films. **c**, Region of photoluminescence tuning for films with different *X*-MBA⁺ ligands. **d**, **e**, Binding energies (*E*ᵦ) of single ligand adsorption *E*ᵦ (**d**) and multiple ligand adsorption barriers (Δ*E*ᵦ; **e**) of the ligands on perovskite surface. **f**, Schematic illustration of the ligand adsorption process.

As shown in Fig. 1d, photoluminescence and absorption spectra show that the bandgap of the Br-MBA⁺ film broadens when the Br-MBA⁺ ligand concentration is increased. We achieve the maximum film bandgap of 2.68 eV, well above the CsPbBr₃ bandgap of 2.37 eV (ref. [28]). The photoluminescence wavelength tuning of the films is continuous, with steps as fine as approximately 2 nm. This continuous tuning distinguishes the materials from 2D and quasi-2D layered perovskites, which have discrete bandgap increments[29,30].

GIWAXS and X-ray diffraction (XRD) measurements (Fig. 1e and Extended Data Fig. 1b) show diffraction peaks indexed to the cubic CsPbBr₃. The low-dose high-resolution transmission electron microscopy (HRTEM) image of a QD in Fig. 1g agreed well with the cubic phase of CsPbBr₃ (ref. [31,32]). Fast Fourier transform analysis indicates the perovskite along the [100] zone axis. The average nanoparticle diameter is 3.5 nm for 2.68-eV emitters, approximately 4.2 nm for 2.59-eV emitters, and approximately 6.4 nm for 2.41-eV emitters. The progressive decrease in size agrees with the blue shift in the photoluminescence that is seen with increased ligand concentration. (Extended Data Fig. 2). Transient absorption spectra display a single narrow bleach peak, and the bleach wavelengths keep constant in time, indicating the nature of the films' monodispersity (Fig. 1f and Extended Data Fig. 4). We fabricate films on diverse substrates and surfaces (Supplementary Note 2), finding that the films have substantially substrate-independent properties. In addition, CsPbI₃ QD films with controllable photoluminescence wavelength could be produced by using Br-DMA⁺ ligands (bromide-substituted DMA⁺; Extended Data Fig. 1 and Supplementary Note 3).

We study CsPbBr₃ QD formation with the aid of synchrotron-based in situ GIWAXS. As shown in Fig. 2a, three distinct stages of film growth

are identified. The broad and weak scattering ring at $q_r \approx 0.43$ Å⁻¹ emerges first and is assigned to the precursor solution[22]. After antisolvent drip, a new diffraction peak at $q_r \approx 0.76$ Å⁻¹ arises, one we assign to the intermediate phase, PbBr₂−2·DMSO, made up of PbBr₂ and DMSO[33,34] (Extended Data Fig. 5). A phase transformation is observed upon heating, with three distinct peaks indexed to the cubic CsPbBr₃ phase progressively appearing and intensifying. The metastable intermediate phase and corresponding controllable crystallization process may contribute to the growth of CsPbBr₃ QDs with a narrow size distribution[19,35] (Supplementary Note 4).

We use in situ photoluminescence spectra to study bandgap evolution during film growth. As shown in Fig. 2b, the initial photoluminescence peak position is correlated with ligand concentration, that is, the higher concentration leads to smaller particles. The photoluminescence position is substantially constant across the duration of the synthesis process, a finding that we attribute to strong binding affinity of the ligands. We propose that strong anchoring affinity of the ligands, as well as control over ligand concentration, are key factors in the crystallization process during SoS that allow the production of QD exhibiting tunable size[36,37] (Supplementary Notes 4, 5).

Focusing further on the role of the tail group, we synthesized several different halide-substituted MBA⁺ ligands, *X*-MBA⁺ (*X* = F, Cl, I), and found that the maximum extent of quantum confinement greatly differed as a function of halide selection (Fig. 2c and Extended Data Fig. 6). From DFT, we project that MBA⁺ will exhibit a lower binding energy (*E*ᵦ = −0.637 eV) compared to the other ligands (Fig. 2d), indicating weaker binding ability and a lower tendency to form small particles[38]. We then consider the case of multiple-ligand adsorption, because the
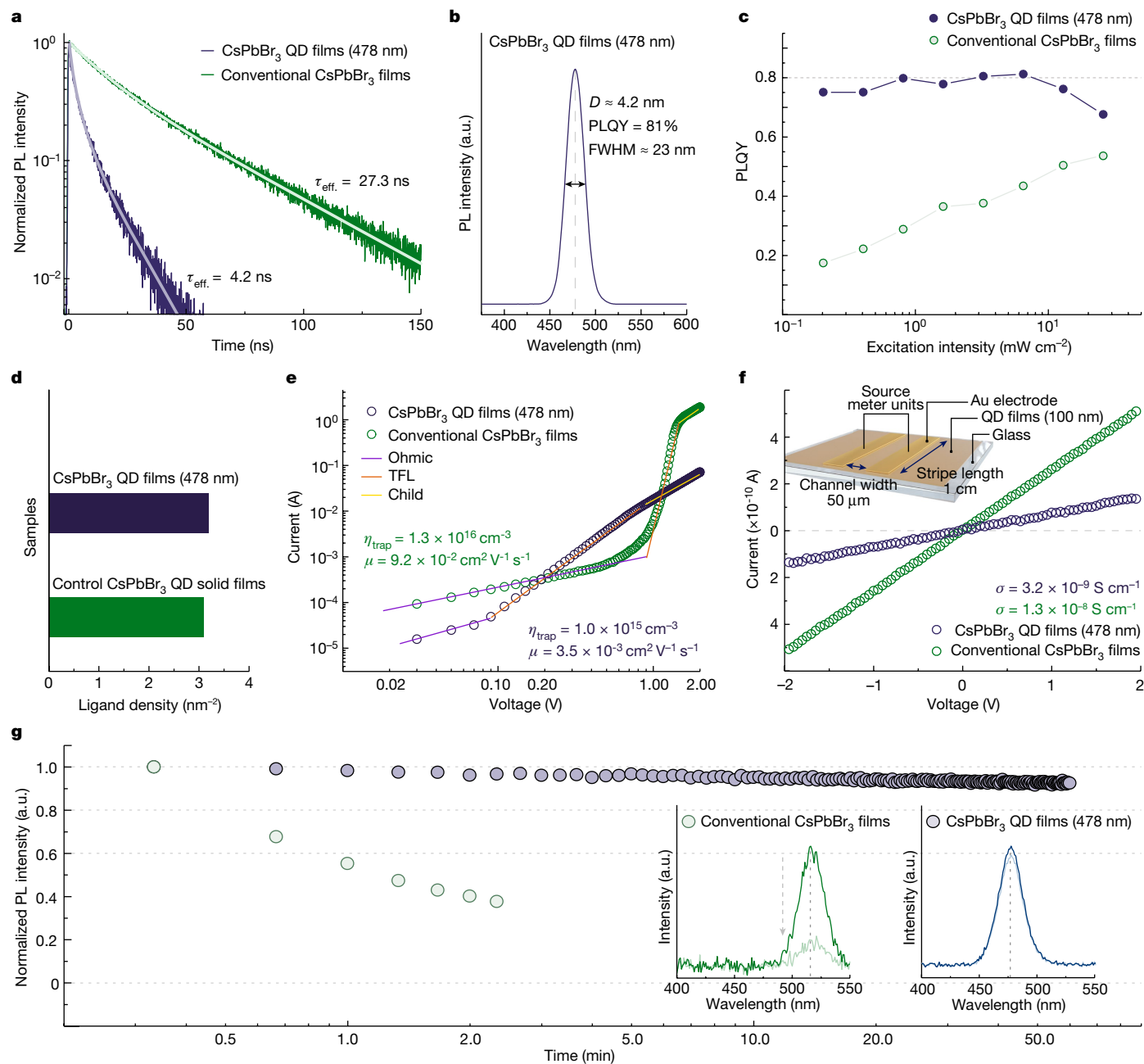
**Fig. 3 | Optical and electrical properties of SoS of QD films. a**, Time-resolved photoluminescence (TRPL) spectra for CsPbBr₃ QD films (478 nm) and conventional CsPbBr₃ films. **b**, Photoluminescence (PL) spectrum of the film under ~3.2 mW cm⁻² excitation. **c**, Photoluminescence quantum yield (PLQY) as a function of excitation intensity for the films. **d**, Surface ligand densities of the film and control sample. **e**,**f**, Space charge-limited current (SCLC; **e**) and conductivity measurements (**f**) for the QD films and conventional CsPbBr₃ films; SCLC measurement (**e**) identified three transition regimes: Ohmic, trap-filled limit (TFL), and Child. **g**, Thermal photoluminescence stability under continuous annealing at 80 °C. Inset, initial photoluminescence spectra of the QD and conventional CsPbBr₃ films (darker lines), and after 60 min (lighter lines).

surface ligand densities are high. We define the adsorption barrier ($\Delta E_b$) as the difference in $E_b$ between single- and multiple-adsorption mode (Fig. 2f). As shown in Fig. 2e, F-MBA⁺ ligands display higher $\Delta E_b$ (0.44 eV for full adsorption) compared to other ligands (approximately 0.35 eV), suggesting it is hard to adsorb multiple F-MBA⁺ ligands on CsPbBr₃ surface. The highly electronegative nature of fluoride enables hydrogen bond (N−H···F) formation between adjacent ligands, inhibiting continuous ligand adsorption[1]. The tail groups thus influence ligand surface binding affinity, with high $E_b$ and low $\Delta E_b$ facilitating strongly confined QD formation. Ab initio molecular dynamics shows that the Br-MBA⁺ ligands form a stable network on perovskites, reflecting strong surface binding (Supplementary Note 5). We note that I-MBA⁺ ligands exhibit

a similar anchoring ability to that of Br-MBA⁺, and result in monodispersed QD films with tunable particle size (Supplementary Note 6).

We obtain an estimate of exciton binding energy ($E_{xb}$) from temperature-dependent photoluminescence measurements (Supplementary Note 7). Given the possibility of structural transition at low temperature, $E_{xb}$ of the perovskites, extracted from photoluminescence measurements, has the potential to be overestimated[39,40]. The blue films exhibit decreased effective photoluminescence lifetime ($\tau_{eff.}$ approximately 4 ns) compared to conventional CsPbBr₃ perovskite (approximately 27 ns), attributed to strong first-order exciton recombination[41] (Fig. 3a). The blue QD films display photoluminescence quantum yield (PLQY) of 80% and FWHM ≈ 23 nm (Fig. 3b). The PLQY is independent
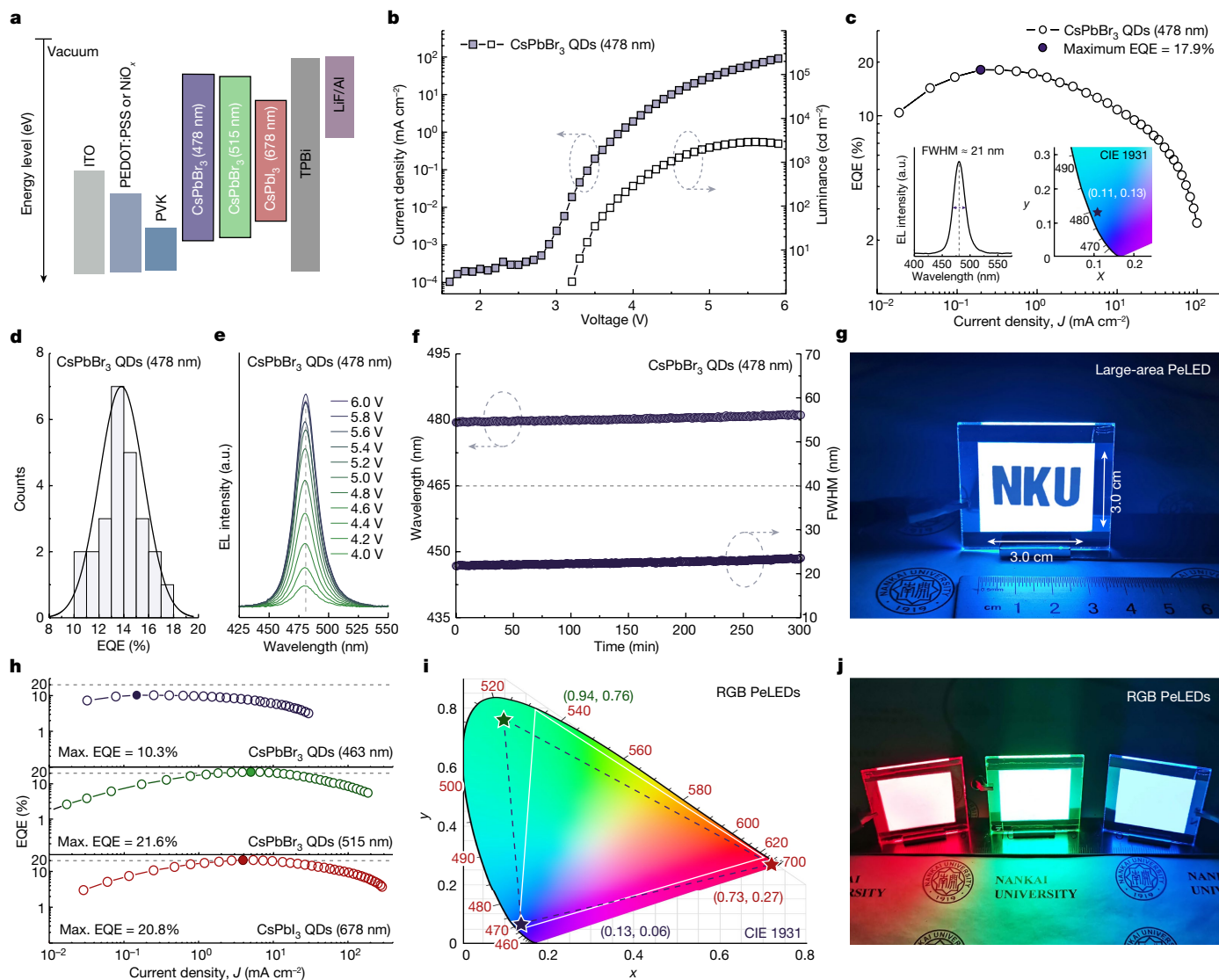
**Fig. 4 | PeLED performance and operating stability. a,** Energy level of each layer in PeLEDs. ITO, indium tin oxide; PEDOT:PSS, poly(3,4-ethylenedioxythiophene): poly(styrene-sulfonate); PVK, Poly(9-vinylcarbazole); TPBi, 1,3,5-Tris(1-phenyl-1H-benzimidazol-2-yl)benzene. **b,c,** $J-V-L$ (filled squares indicate the current density evolution, hollow squares indicate the luminance evolution) (**b**) and corresponding EQE–$J$ (**c**) curves for the PeLEDs based on $CsPbBr_3$ QDs (478 nm). In **c**, the filled symbol indicates the maximum EQE, 17.9%. Inset to **c**, electroluminescence (EL) spectrum (left) and corresponding CIE coordinates, (0.11, 0.13) (right). **d,** Histogram of PeLEDs based on $CsPbBr_3$ QDs (478 nm). **e,** Electroluminescence spectra of PeLEDs operating at different voltages. **f,** Electroluminescence peak position (darker circles) and FWHM (lighter circles) evolution for the PeLEDs. **g,** Photograph of the large-area blue PeLED. **h,** EQE–$J$ curves for blue (top), green (middle) and red (bottom) PeLEDs. The filled symbol indicates the maximum EQEs of 10.3%, 21.6% and 20.8%, respectively. **i,** The CIE coordinates corresponding to the blue, green and red PeLEDs in **h**; the white triangle gives the colour range suggested by International Telecommunication Union (ITU) Recommendation BT.2100-2 (ref. [45]). **j,** Photograph of red–green–blue (RGB) PeLEDs with different QD films.

of the excitation density (Fig. 3c), implying a low defect density. Space charge-limited current (SCLC) measurements revealed a trap state density ($\eta_{trap}$) of $10^{15}$ cm$^{-3}$ (Fig. 3e), lower than in conventional $CsPbBr_3$ films (approximately $10^{16}$ cm$^{-3}$). We extracted carrier mobility using SCLC and found a hole mobility of $\mu = 3 \times 10^{-3}$ cm$^2$ V$^{-1}$ s$^{-1}$, comparable to conventional $CsPbBr_3$ films (Fig. 3e). The film exhibits similar conductivity ($\sigma$) to that of conventional $CsPbBr_3$ (Fig. 3f). We studied the surface-bound ligand density through inductively coupled plasma atomic absorption spectroscopy (ICP-AES), nuclear magnetic resonance (NMR) and X-ray photoelectron spectroscopy (XPS) analysis[42,43] (Supplementary Note 8); we obtained a surface-bound ligand density of 3.2 nm$^{-2}$, similar to control $CsPbBr_3$ QDs after post-washing (3.1 nm$^{-2}$) (Fig. 3d).

We then assess QD film thermal stability under continuous heating at 80 °C: by recording the photoluminescence intensities of the films

as a function of time (Fig. 3g), we find that control $CsPbBr_3$ films suffer from thermal quenching[44]. The $CsPbBr_3$ QD film samples retain PLQY above 90% over 60 min at 80 °C.

We fabricated primary blue PeLEDs (wavelength of less than or equal to 480 nm, with chromaticity with a CIE 1931 colour space $y$-coordinate value less than or equal to 0.13), which, have had a highest reported external quantum efficiency (EQE) of 12.3% (ref. [7]) using the above QD films (Fig. 4a and Extended Data Fig. 7). The LED performance (Fig. 4b,c) shows a maximum EQE of 17.9%, with the electroluminescence (EL) peak at 480 nm and a FWHM of approximately 21 nm, corresponding to the CIE colour-space coordinate (0.11, 0.13). To our knowledge, this is the highest EQE obtained for primary blue PeLEDs, by a factor of 1.5. Fabrication reproducibility is reported in a histogram (Fig. 4d, Extended Data Fig. 9 and Supplementary Note 9).

# Article

The electroluminescence spectra remain the same at different applied voltages (Fig. 4e). We assessed the lifetime of the device by applying a constant current and monitoring the evolution of luminance (Fig. 4f): the electroluminescence wavelength and FWHM remain constant over 5 h at a constant driving current. The operating half lifetime ($T_{50}$) at an initial luminance of 100 cd m$^{-2}$ is 2 h (Extended Data Fig. 8), approximately 5× higher than the best reported efficient blue PeLEDs[7] (Extended Data Table 1). Considering the low glass-transition temperature of the organic carrier transport layer, we suggest that all-inorganic device stacks may offer opportunities for increased operating stability.

To pursue the less than or equal to 465 nm emission needed by the Telecommunication Union (ITU) Recommendation BT.2100-2 standard[45], and noting that the best prior PeLEDs showed EQE in this spectral range of 5% (ref. [12]), we fabricated deep-blue PeLEDs using films with CsPbBr$_3$ QDs of about 3.5 nm, and obtained an EQE of 10.3% with an electroluminescence peak at 465 nm and a FWHM of 23 nm, and CIE coordinates (0.13, 0.06) (Fig. 4g,h and Extended Data Fig. 8). This increases twofold the EQE of PeLEDs compared to those of similar-wavelength previous perovskites.

We also fabricate green-emitting and red-emitting PeLEDs; these have EQEs of 21.6% for 515 nm and 20.8% for 679 nm, respectively (Extended Data Fig. 9). Additionally, we construct RGB PeLEDs with active areas of 3 × 3 cm$^2$ (Fig. 4i,j); these showcase good uniformity in film thickness, roughness and optical properties.

## Online content

Any methods, additional references, Nature portfolio reporting summaries, source data, extended data, supplementary information, acknowledgements, peer review information; details of author contributions and competing interests; and statements of data and code availability are available at https://doi.org/10.1038/s41586-022-05486-3.

1. Ma, D. et al. Distribution control enables efficient reduced-dimensional perovskite LEDs. *Nature* **599**, 594–598 (2021).
2. Lin, K. et al. Perovskite light-emitting diodes with external quantum efficiency exceeding 20 per cent. *Nature* **562**, 245–248 (2018).
3. Cao, Y. et al. Perovskite light-emitting diodes based on spontaneously formed submicrometre-scale structures. *Nature* **562**, 249–253 (2018).
4. Hassan, Y. et al. Ligand-engineered bandgap stability in mixed-halide perovskite LEDs. *Nature* **591**, 72–77 (2021).
5. Chiba, T. et al. Anion-exchange red perovskite quantum dots with ammonium iodine salts for highly efficient light-emitting devices. *Nat. Photonics* **12**, 681–687 (2018).
6. Liu, Y. et al. Efficient blue light-emitting diodes based on quantum-confined bromide perovskite nanostructures. *Nat. Photonics* **13**, 760–764 (2019).
7. Dong, Y. et al. Bipolar-shell resurfacing for blue LEDs based on strongly confined perovskite quantum dots. *Nat. Nanotechnol.* **15**, 668–674 (2020).
8. Shamsi, J. et al. To nano or not to nano for bright halide perovskite emitters. *Nat. Nanotechnol.* **16**, 1164–1168 (2021).
9. Chen, Q. et al. All-inorganic perovskite nanocrystal scintillators. *Nature* **561**, 88–93 (2018).
10. Li, Z. et al. Modulation of recombination zone position for quasi-two-dimensional blue perovskite light-emitting diodes with efficiency exceeding 5%. *Nat. Commun.* **10**, 1027 (2019).
11. Hou, J. et al. Liquid-phase sintering of lead halide perovskites and metal-organic framework glasses. *Science* **374**, 621–625 (2021).
12. Karlsson, M. et al. Mixed halide perovskites for spectrally stable and high-efficiency blue light-emitting diodes. *Nat. Commun.* **12**, 361 (2021).
13. Wang, C. et al. Dimension control of in situ fabricated CsPbClBr$_2$ nanocrystal films toward efficient blue light-emitting diodes. *Nat. Commun.* **11**, 6428 (2020).
14. Nedelcu, G. et al. Fast anion-exchange in highly luminescent nanocrystals of cesium lead halide perovskites (CsPbX$_3$, X = Cl, Br, I). *Nano Lett.* **15**, 5635–5640 (2015).
15. Liu, X. et al. Metal halide perovskites for light-emitting diodes. *Nat. Mater.* **20**, 10–21 (2021).
16. Protesescu, L. et al. Nanocrystals of cesium lead halide perovskites (CsPbX$_3$, X = Cl, Br, and I): novel optoelectronic materials showing bright emission with wide color gamut. *Nano Lett.* **15**, 3692–3696 (2015).
17. Akkerman, Q. A., Raino, G., Kolalenko, M. V. & Manna, L. Genesis, challenges and opportunities for colloidal lead halide perovskite nanocrystals. *Nat. Mater.* **17**, 394–405 (2018).
18. Kovalenko, M. V., Protesescu, L. & Bodnarchuk, M. I. Properties and potential optoelectronic applications of lead halide perovskite nanocrystals. *Science* **358**, 745–750 (2017).
19. Akkerman, Q. A. et al. Controlling the nucleation and growth kinetics of lead halide perovskite quantum dots. *Science* **377**, 1406–1412 (2022).
20. Li, X., Hoffman, J. M. & Kanatzidis, M. G. The 2D halide perovskite rulebook: how the spacer influences everything from the structure to optoelectronic device efficiency. *Chem. Rev.* **121**, 2230–2291 (2021).
21. Miao, Y. et al. In situ growth of ultra-thin perovskitoid layer to stabilize and passivate MAPbI$_3$ for efficient and stable photovoltaics. *eScience* **1**, 91–97 (2021).
22. Munir, R. et al. Hybrid perovskite thin-film photovoltaics: in situ diagnostics and importance of the precursor solvate phases. *Adv. Mater.* **29**, 1604113 (2017).
23. Wang, Y. et al. Chelating-agent-assisted control of CsPbBr$_3$ quantum well growth enables stable blue perovskite emitters. *Nat. Commun.* **11**, 3674 (2020).
24. Ma, D. et al. Chloride insertion-immobilization enables bright, narrowband, and stable blue-emitting perovskite diodes. *J. Am. Chem. Soc.* **142**, 5126–5134 (2020).
25. Lyu, R., Moore, C. E., Liu, T., Yu, Y. & Wu, Y. Predictive design model for low-dimensional organic-inorganic halide perovskites assisted by machine learning. *J. Am. Chem. Soc.* **143**, 12766–12776 (2021).
26. Koegel, A. A. et al. Correlating broadband photoluminescence with structural dynamics in layered hybrid halide perovskites. *J. Am. Chem. Soc.* **144**, 1313–1322 (2022).
27. Xue, J., Wang, R. & Yang, Y. The surface of halide perovskites from nano to bulk. *Nat. Rev. Mater.* **5**, 809–827 (2020).
28. Cui, J. et al. Efficient light-emitting diodes based on oriented perovskite nanoplatelets. *Sci. Adv.* **7**, eabg8458 (2021).
29. Blancon, J., Een, J., Stoumpos, C. C., Kanatzidis, M. G. & Mohite, A. D. Semiconductor physics of organic–inorganic 2D halide perovskites. *Nat. Nanotechnol.* **15**, 969–985 (2020).
30. Peng, X., Wickham, J. & Alivisatos, A. P. Kinetics of II-VI and III-V colloidal semiconductor nanocrystal growth: "focusing" of size distributions. *J. Am. Chem. Soc.* **120**, 5343–5344 (1998).
31. Li, X. et al. Evidence for ferroelectricity of all-inorganic perovskite CsPbBr$_3$ quantum dots. *J. Am. Chem. Soc.* **142**, 3316–3320 (2020).
32. Dong, Y. et al. Precise control of quantum confinement in cesium lead halide perovskite quantum dots via thermodynamic equilibrium. *Nano Lett.* **18**, 3716–3722 (2018).
33. Yang, W. et al. High-performance photovoltaic perovskite layers fabricated through intramolecular exchange. *Science* **348**, 1234–1237 (2015).
34. Baranyi, A. D., Onyszchuk, M., Page, Y. L. & Donnay, G. The crystal and molecular structure of lead (II) bromide-bis-dimethylsulphoxide, PbBr$_2$·2[(CH$_3$)$_2$SO]. *Can. J. Chem.* **55**, 849–855 (1977).
35. Lamer, V. & Dinergar, R. Theory, production and mechanism of formation of monodispersed hydrosols. *J. Am. Chem. Soc.* **72**, 4847–4854 (1950).
36. Huang, H. et al. Growth mechanism of strongly emitting CH$_3$NH$_3$PbBr$_3$ perovskite nanocrystals with a tunable bandgap. *Nat. Commun.* **8**, 996 (2017).
37. Lifshitz, I. M. & Slyozov, V. V. The kinetics of precipitation from supersaturated solid solutions. *J. Phys. Chem. Solids* **19**, 35–50 (1961).
38. Peng, X. et al. Shape control of CdSe nanocrystals. *Nature* **404**, 59–61 (2000).
39. Miyata, A. et al. Direct measurement of the exciton binding energy and effective masses for charge carriers in organic–inorganic tri-halide perovskites. *Nat. Phys.* **11**, 582–587 (2015).
40. D'Innocenzo, V. et al. Excitons versus free charges in organo-lead tri-halide perovskites. *Nat. Commun.* **5**, 3586 (2014).
41. deQuilettes, D. W. et al. Charge-carrier recombination in halide perovskites. *Chem. Rev.* **119**, 11007–11019 (2019).
42. Xue, J. et al. Surface ligand management for stable FAPbI$_3$ perovskite quantum dot solar cells. *Joule* **2**, 1866–1878 (2018).
43. Hao, M. et al. Ligand-assisted cation-exchange engineering for high-efficiency colloidal Cs$_{1-x}$FA$_x$PbI$_3$ quantum dot solar cells with reduced phase segregation. *Nat. Energy* **5**, 79–88 (2020).
44. Liu, M. et al. Suppression of temperature quenching in perovskite nanocrystals for efficient and thermally stable light-emitting diodes. *Nat. Photonics* **15**, 379–385 (2021).
45. International Telecommunication Union. *Recommendation ITU-R BT.2100-2: Image Parameter Values for High Dynamic Range Television for Use in Production and International Programme Exchange* (ITU, 2018); https://www.itu.int/rec/R-REC-BT.2100-2-201807-I/en.

# Methods

## Materials

All materials were used as received without further purification. Caesium bromide (CsBr), caesium iodide (CsI), lead bromide (PbBr$_2$), lead iodide (PbI$_2$) were purchased from Sigma-Aldrich. Poly(9-vinycarbazole) (PVK), 1,3,5-Tris(1-phenyl-1H-benzimidazol-2-yl)benzene (TPBi) and lithiumfluoride (LiF) were purchased from Lumtec. CsPbBr$_3$ QD solution was purchased from Suzhou Xingshuo Nanotech Co. (product ID: XSNC-20211029-1).

## PeLED fabrication

ITO/NiO$_x$/PVK/perovskite/TPBi/LiF/Al device configuration was used for the blue PeLEDs. Ni(CH$_3$COO)$_2$·4H$_2$O (0.1 M) and NH$_2$CH$_2$CH$_2$OH (0.1 M) were dissolved in ethanol to form a deep-green solution. The solution was spin-coated onto indium tin oxide (ITO) substrates at 2,000 rpm for 60 s, and followed by heating at 275 °C for 45 min. The overlapped PVK layer was deposited from its chlorobenzene solution (4 mg ml$^{-1}$) at 4,000 rpm. Perovskite layers were deposited through a single-step deposition. In particular, the precursor solution was spin-coated at 5,000 rpm for 60 s. After spin-coating for 20 s, 100 μl chlorobenzene was dropped onto the film. Then, the colourless films were annealed at 80 °C for 10 min. 0.3 mg ml$^{-1}$ of tris(4-fluorophenyl) phosphine oxide (TFPPO) in methyl acetate was then spin-coated onto the perovskite film at 4,000 rpm for 1 min. TPBi (40 nm), LiF (0.8 nm) and Al electrodes were evaporated on the top of the device with an effective area of 9.0 mm$^2$. The precursor solutions were prepared according to Supplementary Note 10.

## Characterization of perovskite films

Absorption spectra were recorded from a UV–visible–near-infrared system (LAMBDA 950). Scanning electron microscope (SEM) images were captured by a field-emission SEM (JSM-7500F, JEOL). Atomic force microscope (AFM) images were acquired by Dimension Icon (Bruker) with noncontact mode. XRD patterns of perovskites were obtained using a Rigaku Smart Lab X-ray diffractometer (9 kW) with Cu-Kα sources ($\lambda$ = 0.1542 nm).

## Low-dose transmission electron microscopy analysis

Low-dose HRTEM analysis was performed using JEOL NEOARM 200F with a probe corrector at an acceleration voltage of 80 kV. The HRTEM images were acquired using a direct-detection camera (Gatan K3) operated in electron-counting mode with the dose fractionation function. To avoid possible beam damage and phase transition of perovskite QDs under the electron beam, live time was set to ensure that the dose rate was below 10 $e$ Å$^{-2}$ s$^{-1}$, which is much lower than the reported perovskite decomposition critical dose[46].

## Photoluminescence characterization

Photoluminescence spectra of films were measured on a photoluminescence spectrophotometer (FS5, Edinburgh Instruments). TRPL spectra were recorded through a spectrometer (FLS 980, Edinburgh Instruments). The samples were photoexcited using a 355-nm picosecond pulsed laser with a repetition rate of 800 kHz. A time-correlated single-phono counting system was used to resolve the photoluminescence dynamics with the total instrument response function of less than 100 ps. PLQYs of films were recorded through a three-step technique by a Quanta-Phi integrating sphere with a Fluorolog system. In situ photoluminescence spectra evolution was monitored by using a fibre spectrometer (QE65 Pro spectrometer, Ocean Optics); and the photoluminescence spectra were collected in reflection mode with an optical filter (from 400 to 700 nm). Temperature-dependent photoluminescence spectra were recorded on LabRAM HR800 (Horiba) equipped with a liquid-nitrogen-cooled cryostat (Linkam); a 325-nm laser with a power of 3 μW was used as the excitation source.

## Transient absorption measurement

Transient absorption measurements were performed on a pump-probe system (Helios, Ultrafast Systems) coupled with an amplified femtosecond laser system (Coherent). The white light continuum probe pulse (from 370 nm to 600 nm or from 420 nm to 780 nm) was generated by focusing an 800-nm pulse beam into a CaF$_2$ or a sapphire plate. The pump pulse (pulse width, around 100 fs; pulse energy, 0.2 μJ per pulse; 350 nm or 450 nm) was generated through an optical parametric amplifier (TOPAS-800-fs, Coherent). The instrument response function was determined to be 100 fs. All the transient absorption data were obtained and averaged from at least five scans.

## Grazing-incidence wide-angle X-ray scattering measurements

In situ and ex situ GIWAXS data were collected at beamline BL17B of the Shanghai Synchrotron Radiation Facility (SSRF), China. A monochromatic beam of $\lambda$ = 1.240 Å was used, and the incident angle was around 0.4°. The distance between sample and detector was calibrated with a lanthanum hexaboride (LaB$_6$) sample. Samples were measured under a mild N$_2$ flow. During in situ GIWAXS measurement, the spin-coating and annealing process was conducted using custom-built spin-coating and annealing stages, respectively, which were controlled from a computer outside the chamber. The exposure time of every frame was 1 s during the whole measurement.

## Device characterization

Current density–voltage ($J$–$V$) characteristics of the PeLED devices were monitored in an N$_2$-filled glovebox using a computer-controlled Keithley 2400 source meter unit. The devices were measured from zero bias to forward bias under a scanning rate of 0.1 V s$^{-1}$ with a dwell time of 1 s. The electroluminescence spectra were recorded concurrently with a fibre-coupled spectrometer (QE65 Pro, FOIS-1-FL integration sphere). The integrating sphere-spectrometer system was calibrated by an HL-3P-INT-CAL calibration source (Ocean Optics). The operational lifetime ($T_{50}$) was conducted using the same set-up, but under a constant current density condition. The electroluminescence characteristics of PeLEDs were cross-checked by a system comprising a PR-735 spectroradiometer (Photo Research) coupled with a Keithley 2400 source meter unit.

## DFT calculations

First-principles calculations based on DFT were performed using the Vienna ab initio Simulation Package (VASP)[47]. As the exchange-correlation functional, the generalized gradient approximation of Perdew–Burke–Ernzerhof (PBE) functional was used[48]. For slab calculations, we use the DFT-D3 method for the van der Waals correction and dipole corrections for slab calculations[49]. The plane-wave cut-off energy of 400 eV was used. The energy and force convergence criteria were set to 10$^{-5}$ eV and 0.02 eV Å$^{-1}$, respectively. The binding energies ($E_b$) of different ligands with CsPbBr$_3$ perovskite surface were calculated as $E_{mol/pvsk} - E_{pvsk} - E_{mol}$, where $E_{mol/pvsk}$, $E_{pvsk}$ and $E_{mol}$ are the total energies of the adsorption system, the perovskite system and ligand crystals, respectively. We used a 3 × 3 supercell slab with a vacuum of 20 Å along the $z$ direction. In 2D perovskite formation calculations, the interaction energies ($E_{int}$) of adjacent fragments at their interfaces was defined as[50]: $E_{int} = E_{tot} - E_{fragment1} - E_{fragment2}$, where $E_{tot}$, $E_{fragment1}$ and $E_{fragment2}$ are the total energies of the entire system, and two fragments cut from the optimized system. The formation energies ($E_f$) of 2D perovskites with different layers $n$ are calculated using the following formula[51,52]:

$$E_f = \frac{E_{(PbX_2)_n(CsX)_{n-1}(LX)_2} - nE_{PbX_2} - (n-1)E_{CsX} - 2E_{LX}}{n},$$

$$\Delta E_f(CsPbBr_3) = E_f(PEA) - E_f(MBA),$$

# Article

$$\Delta E_f(CsPbI_3) = E_f(MBA) - E_f(DMA),$$

where $L$ = PEA, MBA, DMA and $X$ = Br, I.

## Data availability

All data generated or analysed during this study are included in the published article and its Supplementary Information. Other data that support the findings of this study are available from the corresponding author upon reasonable request.

46. Chen, S. et al. Atomic scale insights into structure instability and decomposition pathway of methylammonium lead iodide perovskite. *Nat. Commun.* **9**, 4807 (2018).
47. Kresse, G. & Furthmüller, J. Efficient iterative schemes for ab initio total-energy calculations using a plane-wave basis set. *Phys. Rev. B* **54**, 11169–11186 (1996).
48. Perdew, J. P., Burke, K. & Ernzerhof, M. Generalized gradient approximation made simple. *Phys. Rev. Lett.* **77**, 3865–3868 (1996).
49. Lee, K., Murray, É. D., Kong, L., Lundqvist, B. I. & Langreth, D. C. Higher-accuracy van der Waals density functional. *Phys. Rev. B* **82**, 081101 (2010).
50. Proppe, A. H. et al. Multication perovskite 2D/3D interfaces form via progressive dimensional reduction. *Nat. Commun.* **12**, 3472 (2021).
51. Yang, Y., Gao, F., Gao, S. & Wei, S. H. Origin of the stability of two-dimensional perovskites: a first-principles study. *J. Mater. Chem. A* **6**, 14949–14955 (2018).
52. Fu, Y. et al. Stabilization of the metastable lead iodide perovskite phase via surface functionalization. *Nano Lett.* **17**, 4405–4414 (2017).

**Author contributions** M.Y. conceived the idea. M.Y., J.C. and E.H.S. guided the project. Y.J. and M.Y. developed the SoS of QD films. C.S., Yuan Liu and H.W. carried out the device fabrication and characterizations. S.L. and Y.Y. carried out GIWAXS measurements and analyses. Y.J., M.C., C.Q. and Yufang Liu performed transient absorption characterizations and analysed the data. J.X., S.H. and E.H.S carried out theoretical calculations. C.S., K.W., T.Z. and W.Z. carried out the TEM characterization. X.F. and Yaqi Liu helped to synthesize the materials and collect the data. J.Y., S.G. and J.P. contributed to the schematics and photographs. Y.J., J.X., J.C., M.Y. and E.H.S. co-wrote the paper. All authors discussed the results and commented on the manuscript.

**Extended Data Fig. 1 | SoS of RGB QD films. a**, PL and absorption spectra of CsPbBr$_3$ and CsPbI$_3$ QD films fabricated via SoS with various ligand concentrations (from 0 to 0.28 M); inset: photographs of QD films under excitation. Since CsPbI$_3$ suffers from phase stability, we were not able to stabilize ultrasmall CsPbI$_3$ QDs with emission wavelength of below 640 nm. **b**,**c**, XRD patterns of CsPbBr$_3$ (**b**) and CsPbI$_3$ (**c**) QD films. **d**, Transient absorption spectra of CsPbI$_3$ QD films (641 nm).
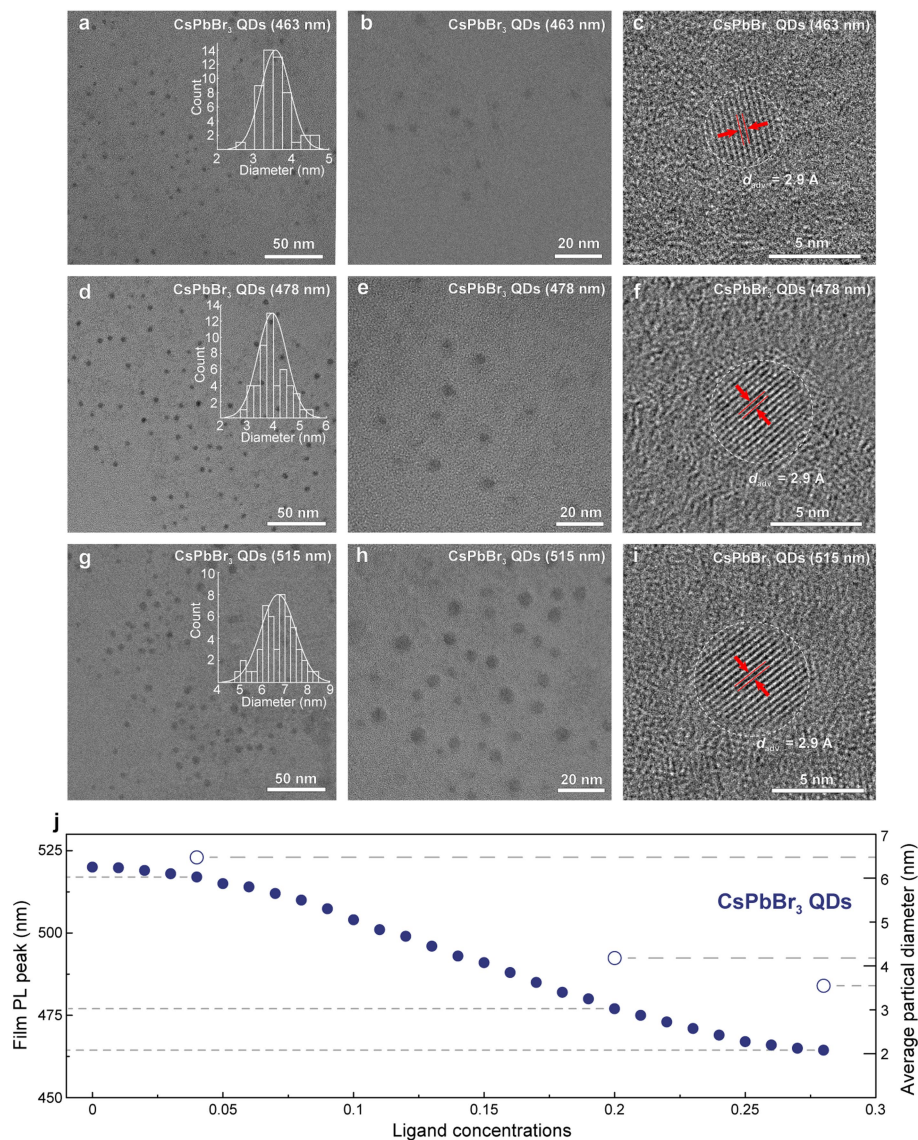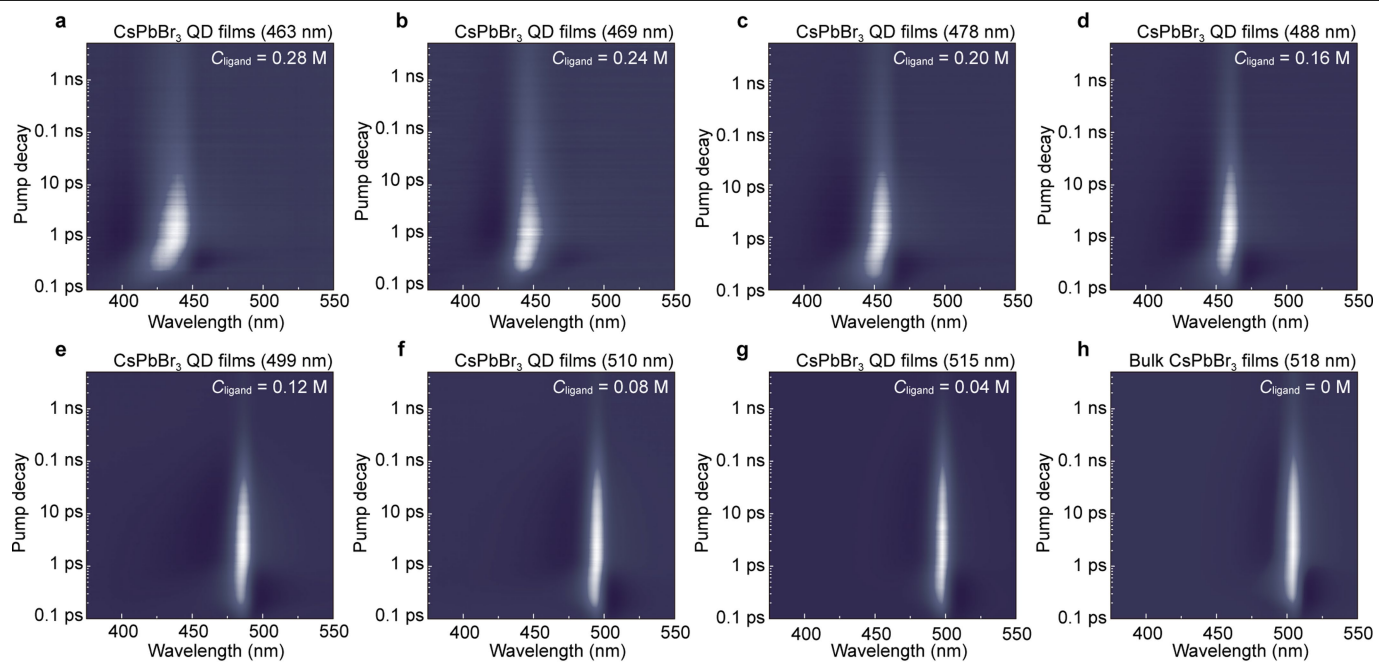
**Extended Data Fig. 2 | TEM characterization for CsPbBr₃ QDs. a–i**, TEM images for CsPbBr$_3$ (463 nm) (**a–c**), CsPbBr$_3$ (478 nm) (**d–f**) and CsPbBr$_3$ (515 nm) (**g–i**) QDs. To avoid possible beam damage and phase transition of perovskite QDs, live time was set to ensure a dose rate of below 10 $e$ Å$^{-2}$ s$^{-1}$. The inter-planar distance was calculated by average distance value ($d_{adv.}$) between five lattice fringes. The statistical diameter histogram was obtained by counting over 50 QDs. **j**, Relationship among ligand concentration, the peak wavelength of QD films and the size of the QDs.
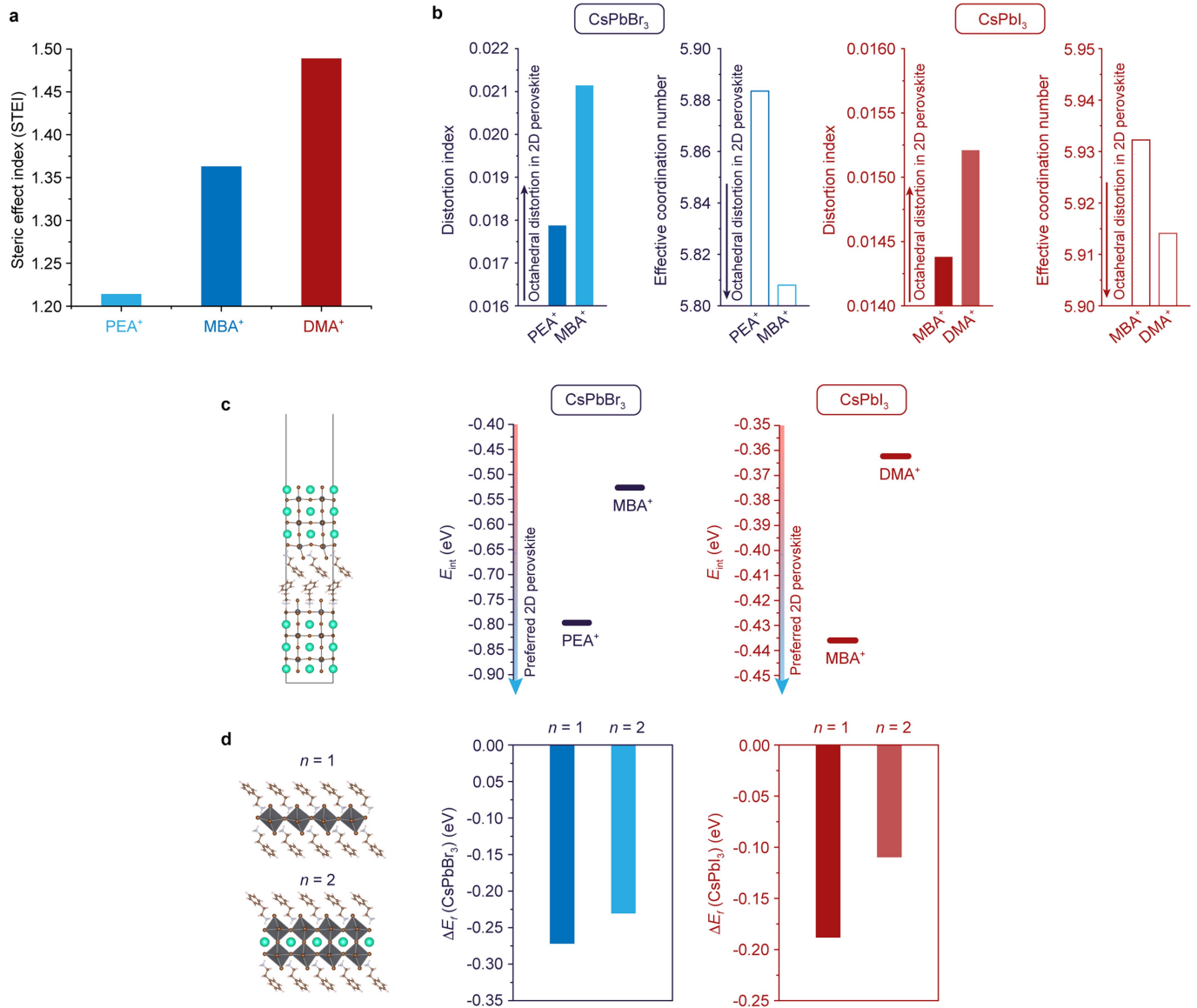
**Extended Data Fig. 3 | 2D formation feasibility of perovskites. a**, Steric effect index (STEI) of PEA+, MBA+ and DMA+ ligands. **b**, Octahedral distortion index and effective coordination number for PEA+- or MBA+- substituted $CsPbBr_3$ (left) and MBA+- or DMA+-substituted $CsPbI_3$ (right) perovskite slabs. **c**, Interaction energies ($E_{int}$) of adjacent fragments at their interfaces for PEA+- or MBA+-substituted $CsPbBr_3$ perovskite slabs and MBA+- or DMA+-substituted $CsPbI_3$ perovskite slabs. **d**, Formation energy differences ($\Delta E_f$) for $CsPbBr_3$ and $CsPbI_3$ layered perovskites with $n$ values of 1 and 2.

**Extended Data Fig. 4 | Transient absorption characterization of CsPbBr₃ QDs. a–h**, Time-wavelength-dependent transient absorption spectra for CsPbBr₃ QD films fabricated via SoS by adding various amounts of ligand (from 0 to 0.28 M).
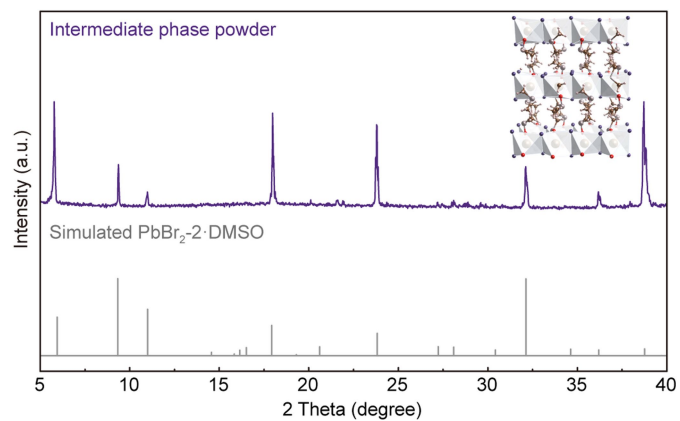
**Extended Data Fig. 5 | XRD pattern of the intermediate phase powder.**
The intermediate phase powder was obtained via the antisolvent-diffusion
method. All the diffraction peaks can be indexed as the $PbBr_2$-$2 \cdot DMSO$ complex.
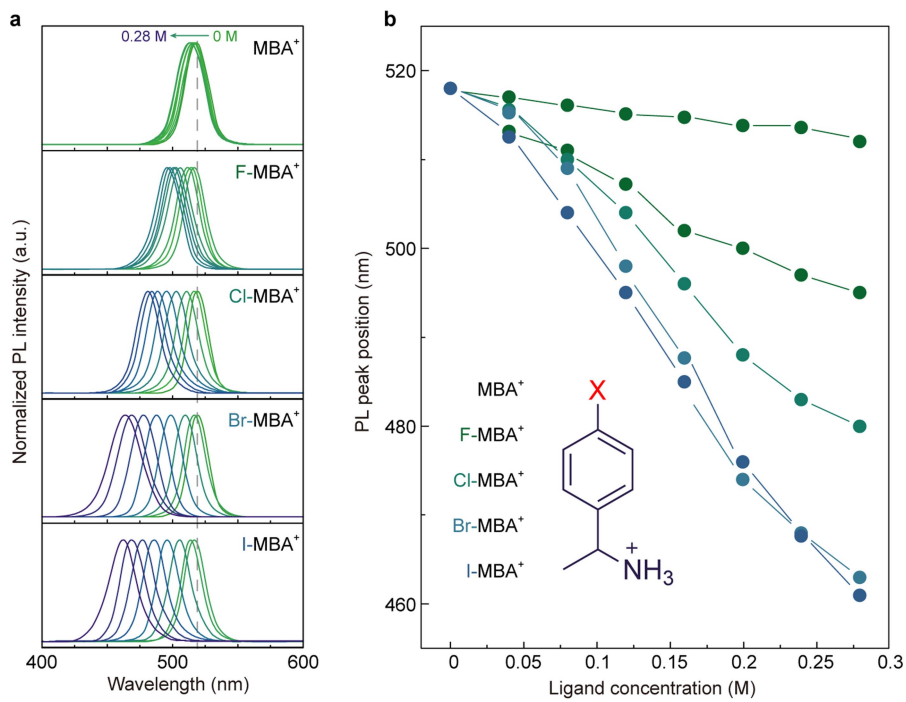
**Extended Data Fig. 6 | Steady-state PL characteristics of CsPbBr₃ QD films with different capping ligands. a,b**, Steady-state PL spectra (**a**) and corresponding PL peak positions (**b**) of CsPbBr₃ perovskite QD films with different *X*-MBA⁺ ligands.

**a** CsPbBr$_3$ QD films (463 nm)

**b** CsPbBr$_3$ QD films (478 nm)

**c** CsPbBr$_3$ QD films (515 nm)

1 µm

**d** CsPbBr$_3$ QD films (463 nm)

r.m.s. = 1.01 nm

**e** CsPbBr$_3$ QD films (478 nm)

r.m.s. = 0.89 nm

**f** CsPbBr$_3$ QD films (515 nm)

r.m.s. = 1.83 nm
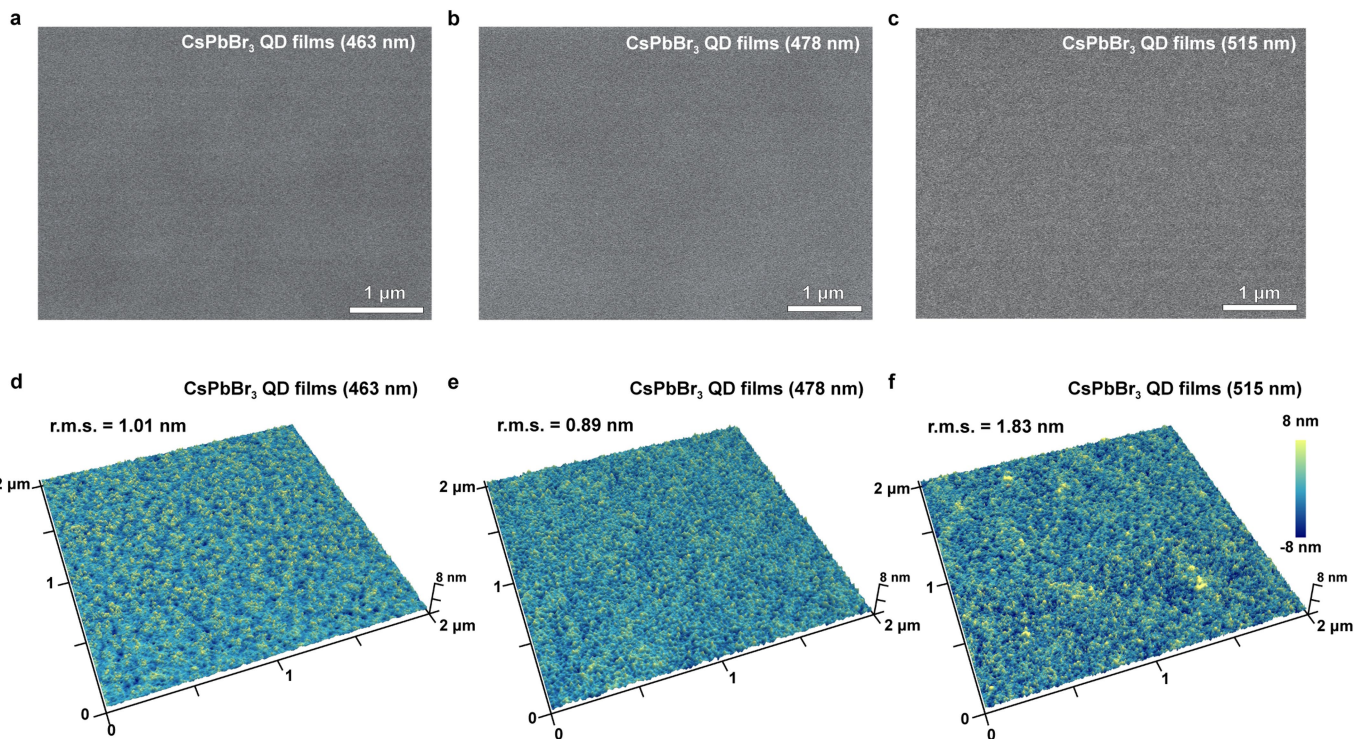
**Extended Data Fig. 7 | Morphological properties of perovskite QD films. a–f**, SEM (**a–c**) and AFM (**d–f**) images for CsPbBr$_3$ (463 nm; **a,d**), CsPbBr$_3$ (478 nm; **b,e**) and CsPbBr$_3$ (515 nm; **c,f**) QD films. r.m.s., root mean square.
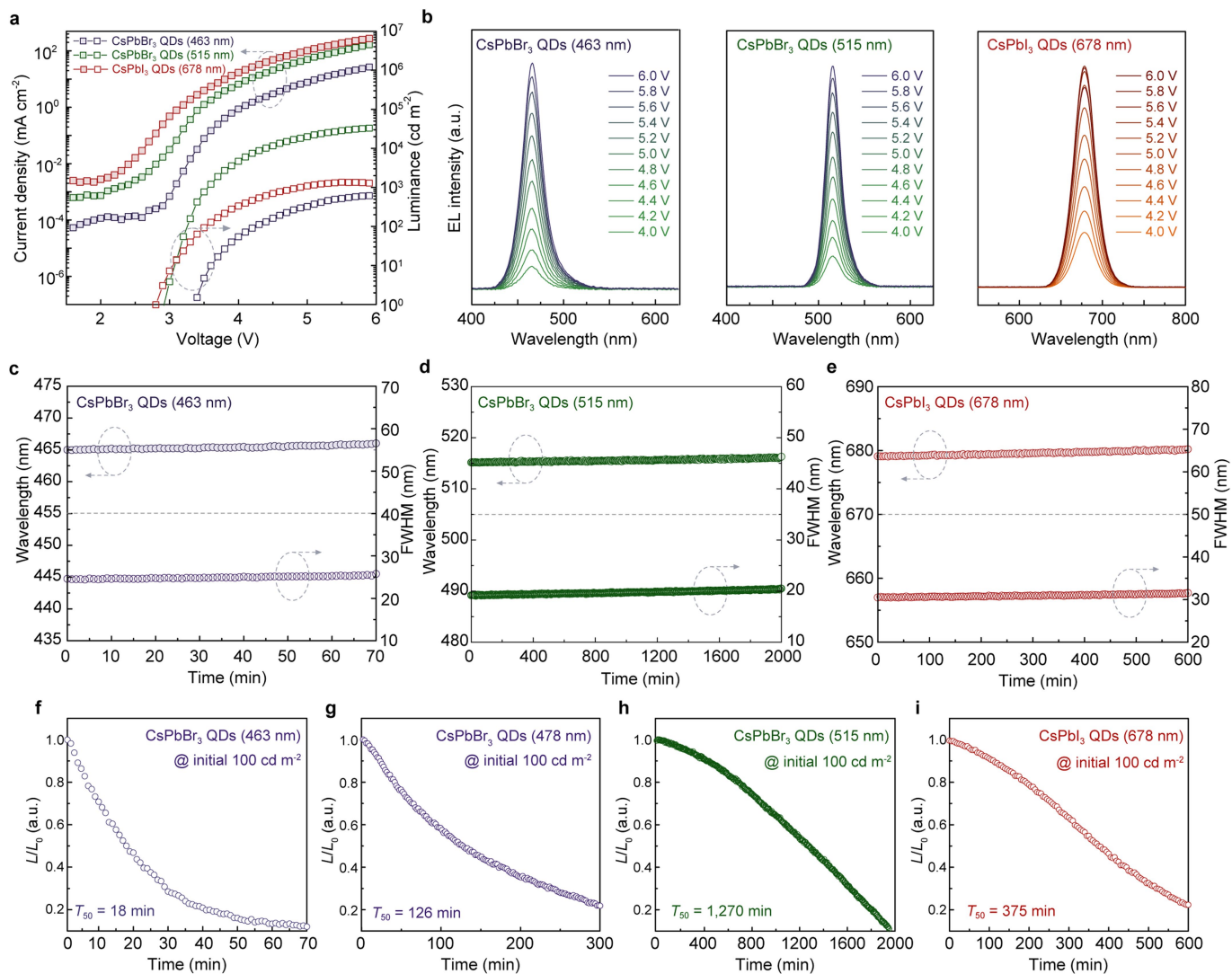
**Extended Data Fig. 8 | EL performance of RGB PeLEDs. a**, *J*–*L*–*V* curves of the RGB PeLEDs. **b**, EL spectra of the PeLEDs operating at different voltages. **c**–**e**, EL peak position and FWHM evolution as a function of time for the PeLEDs. The operational stability measurement was carried out with initial luminance of -100 cd m⁻². **f**–**i**, Half-lifetime ($T_{50}$) measurements for the PeLEDs.
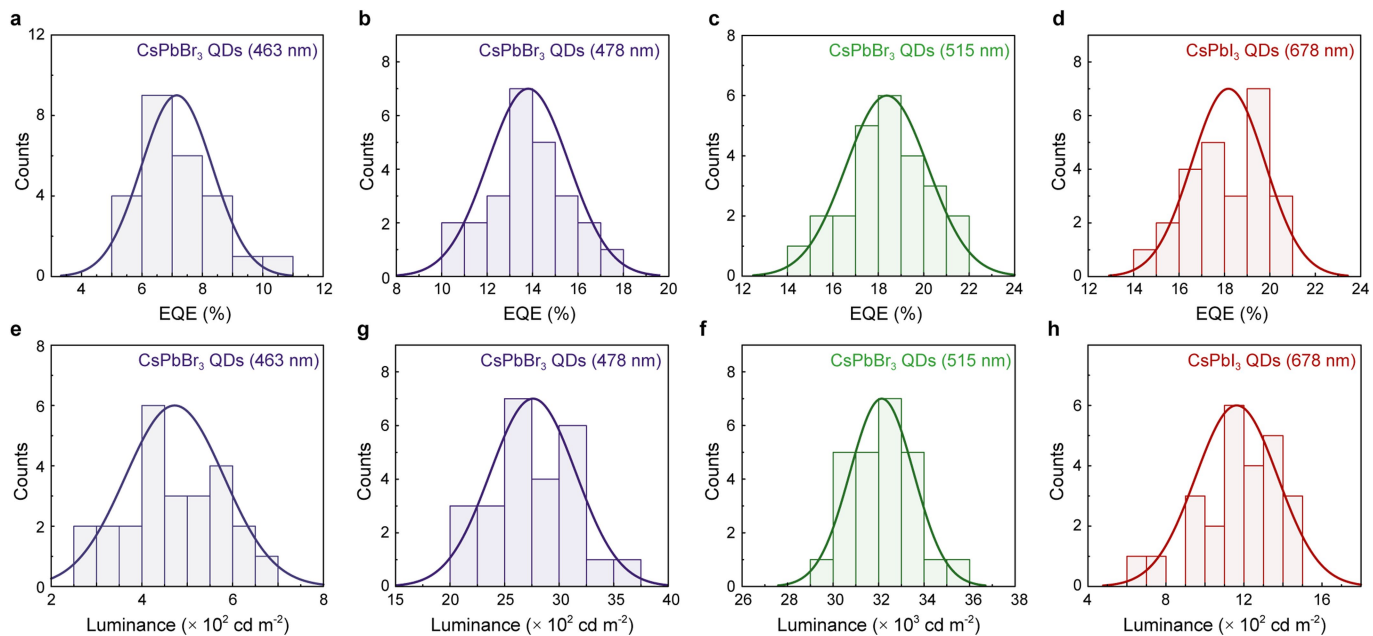
**Extended Data Fig. 9 | Histogram of PeLEDs. a–h**, Histograms of peak EQEs (**a–d**) and maximum luminance (**e–h**) values for the PeLEDs based on CsPbBr₃ (463 nm; **a,e**), CsPbBr₃ (478 nm; **b,g**), CsPbBr₃ (515 nm; **c,f**), and CsPbI₃ (678 nm; **d,h**) QDs. Detailed data have been provided in Supplementary Note 9.

# Article

**Extended Data Table 1 | Summary of efficient blue PeLEDs (EQE > 5%) reported to date Refs.** [6,7,12,13,23,24]

## Deep-blue PeLEDs (< 470 nm)

| Types of perovskites | EL | Peak EQE | Max. Lum. | $T_{50}$ | Ref. |
|---|---|---|---|---|---|
| Mixed halide perovskite | 467 nm | 5.5% | 330 cd m$^{-2}$ | *none* | *Nat. Commun.* **2021**, 12, 361 |
| **CsPbBr$_3$ QDs** | **465 nm** | **10.3%** | **576 cd m$^{-2}$** | **18 min @ 100 cd m$^{-2}$** | ***This work*** |

## Primary-blue PeLEDs (470 - 480 nm)

| Types of perovskites | EL | Peak EQE | Max. Lum. | $T_{50}$ | Ref. |
|---|---|---|---|---|---|
| Mixed halide perovskite | 473 nm | 8.8% | 482 cd m$^{-2}$ | 6.3 min @ 100 cd m$^{-2}$ | *Nat. Commun.* **2020**, 11, 6428 |
| Mixed halide perovskite | 477 nm | 11% | 2,180 cd m$^{-2}$ | 87 s @ 5 mA cm$^{-2}$ | *Nat. Commun.* **2021**, 12, 361 |
| Layered perovskite | 478 nm | 6.3% | < 200 cd m$^{-2}$ | 150 s @ 200 cd m$^{-2}$ | *Nat. Commun.* **2020**, 11, 3674 |
| Layered perovskite | 479 nm | 5.2% | 468 cd m$^{-2}$ | 90 min @ 100 cd m$^{-2}$ | *J. Am. Chem. Soc.* **2020**, 142, 5126 |
| (Cs/FA)PbBr$_3$ QDs | 478 nm | 6.3% | ~ 400 cd m$^{-2}$ | *none* | *Nat. Photonics* **2019**, 13, 760 |
| CsPbBr$_3$ QDs | 479 nm | 12.3% | ~ 400 cd m$^{-2}$ | 20 min @ 90 cd m$^{-2}$ | *Nat. Nanotechnol.* **2020**, 15, 668 |
| (Cs/FA)PbBr$_3$ QDs | 483 nm | 9.5% | ~ 700 cd m$^{-2}$ | 250 s @ 100 cd m$^{-2}$ | *Nat. Photonics* **2019**, 13, 760 |
| **CsPbBr$_3$ QDs** | **480 nm** | **17.9%** | **2,910 cd m$^{-2}$** | **126 min @ 100 cd m$^{-2}$** | ***This work*** |